batteries

MDPI

Review

Critical Challenges and Recent Advances Toward Practical Room-Temperature Sodium–Sulfur Batteries

Zhijiang Su [1], Simeng Tian [2], Xuechao Yang [3], Qi Wang [3], Jia Chang [3], Dalong Zhong [1], Chunwei Dong [1,*], Yang Dong [1,*] and Xiaoxiao Liang [4,*]

[1] National Institute of Clean-and-Low-Carbon Energy, Future Science & Technology City, Changping District, Beijing 102209, China
[2] School of Textile and Materials Engineering, Dalian Polytechnic University, Dalian 116034, China
[3] CHN Energy Yulin Chemical Co., Ltd., Qingshui Coal Chemical Park, Yushen Industrial Zone, Shenfueconomic Development Zone, Yulin 719302, China
[4] State Key Laboratory of Tropical Ocean Engineering Materials and Materials Evaluation, School of Marine Technology and Equipment and School of Materials Science and Engineering, Hainan University, Haikou 570228, China
* Correspondence: 20066669@chnenergy.com.cn (C.D.); 17240043@ceic.com (Y.D.); 997206@hainanu.edu.cn (X.L.)

Abstract

Room-temperature sodium–sulfur (RT Na–S) batteries are gaining renewed interest as a cost-effective, high-energy-density candidate for next-generation storage, owing to their high theoretical specific energy (1274 Wh kg^{-1}) and the earth abundance of sodium. However, their practical application continues to be hampered by persistent challenges such as the polysulfide shuttle effect, uncontrolled growth of sodium (Na) dendrites and electrolyte-induced interfacial instability. This review summarizes recent progress in several key areas: cathode design (including defect engineering, single-atom catalysts, heterostructures), anode interfacial regulation (through SEI/CEI engineering and additive chemistry), and electrolyte formulation (notably localized high-concentration electrolytes and solvation-structure tuning). Although promising results have been achieved at the laboratory scale, critical challenges remain for practical deployment, particularly under high-sulfur-loading and lean-electrolyte conditions, along with fundamental interfacial issues inherent to all-solid-state battery architectures.

Keywords: room-temperature Na–S batteries; sodium polysulfide; shuttle effect; electrochemical performance; optimizing strategy

Check for updates

Academic Editor: Torsten Brezesinski

Received: 6 May 2026
Revised: 11 August 2026
Accepted: 13 August 2026
Published: 1 November 2026

Copyright: © 2026 by the authors. Licensee MDPI, Basel, Switzerland. This article is an open access article distributed under the terms and conditions of the Creative Commons Attribution (CC BY) license.

1. Introduction

Sodium-sulfur batteries offer a theoretical specific energy of 1274 Wh kg^{-1}—approximately three times that of conventional lithium-ion systems (~420 Wh kg^{-1}) [1]—while relying on sodium, an element about 1180 times more abundant in the earth than lithium [2,3]. Consequently, the raw material cost of sodium is only about 1/25 that of lithium, making RT Na–S batteries chemistry an inherently low-cost, high-energy platform for grid storage and mobility applications. Historically, Na–S batteries technology was demonstrated in the 1960s as a high-temperature (300–350 °C) system employing molten electrodes and β″-alumina solid electrolytes [4,5]. Although commercialized for stationary storage, its widespread adoption has been limited by the need for thermal management, corrosion challenges, and safety concerns associated with molten sulfur and sodium [6,7]. Over the past decade, research efforts have therefore shifted toward room-temperature operation,

where polymer-gel or liquid organic electrolytes enable sufficient Na^+ conductivity under ambient conditions.

A typical room-temperature Na–S cell consists of a metallic sodium anode, a sulfur/carbon composite cathode, and an ion-conducting electrolyte [8]. During discharge, solid S_8 undergoes ring-opening to form soluble long-chain sodium polysulfides (Na_2S_8), which are then progressively reduced to shorter-chain species and eventually to insulating Na_2S [9]. The charge process reverses these steps; however, the intermediate polysulfides tend to shuttle between electrodes, leading to rapid capacity fade and low Coulombic efficiency. Since the first RT Na–S prototype was reported in 2006 [10], considerable advances have been made in cathode nanoengineering, anode interfacial protection, and electrolyte design. Nevertheless, the complex interplay between sulfur redox chemistry and interfacial stability remains a critical challenge for practical implementation. The configuration and working principle of such a typical RT Na–S coin cell are illustrated in Figure 1.

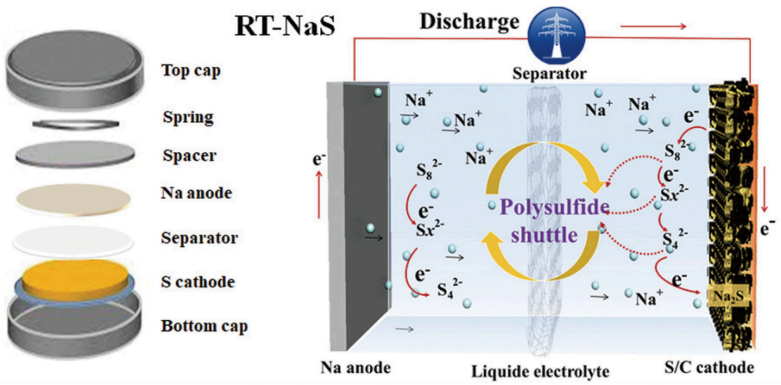


Figure 1. Configuration of a representative coin cell and schematic operation of an RT Na–S batteries. Reproduced with permission [8], Copyright 2020, WILEY–VCH.

Several authoritative reviews have established the fundamental cell chemistry and catalogued cathode, electrolyte, separator, and anode strategies for RT Na–S batteries [2,4]. The present review is differentiated by a problem-centred framework that links molecular-scale sulfur speciation to electrode-scale transport, Na-metal inventory loss, and full-cell constraints. We therefore evaluate not only whether a material improves capacity or cycling in a coin cell, but also whether the underlying strategy remains credible at sulfur loadings ≥ 5 mg cm^{-2}, E/S ratios ≤ 5 μL mg^{-1}, limited Na excess (preferably $N/P \leq 3$), and pouch- or full-cell formats. These thresholds are used as working screening criteria rather than universal standards, because the optimal values remain chemistry- and architecture-dependent.

2. Working Principles and Challenges of RT Na–S Batteries

RT Na–S batteries operate via a reversible two-electron reaction between metallic sodium and elemental sulfur, enabling the interconversion of electrical and chemical energy. This conversion process is inherently complex, involving sequential electron transfers and concurrent phase transitions. Consequently, a majority of the persistent challenges in these batteries arise from the electrochemical evolution of both electrodes during cycling. A primary source of degradation is the dissolution and migration of soluble polysulfides at the cathode.

2.1. Electrochemical Mechanism of RT Na–S Batteries

RT Na–S batteries offer a high theoretical specific capacity of 1675 mAh g^{-1} and a theoretical energy density of 1274 Wh kg^{-1}, which originate from the reversible electrochemical reactions at both electrodes [11]. The overall cell reaction can be summarized as:

$$S_8 + 16Na^+ + 16e^- \rightarrow 8Na_2S \quad (1)$$

The cathodic transformation from elemental S_8 to the final discharge product, Na_2S, is intrinsically complex, which typically begins with the ring-opening of S_8 and proceeds through sodium polysulfide intermediates of varying chain lengths. The electrochemical behavior of RT Na–S batteries is highly electrolyte-dependent, exhibiting pronounced differences between ether-based and carbonate-based liquid electrolytes. In ether-based electrolytes, sulfur conversion generally follows a solid–liquid–solid dissolution–precipitation pathway. Crystalline S_8 first forms soluble long-chain Na_2S_n species, which are subsequently reduced through shorter-chain intermediates before Na_2S_2/Na_2S precipitation. Accordingly, the discharge profile of S_8 exhibits two distinct voltage plateaus separated by two sloping regions, as illustrated in Figure 2a.

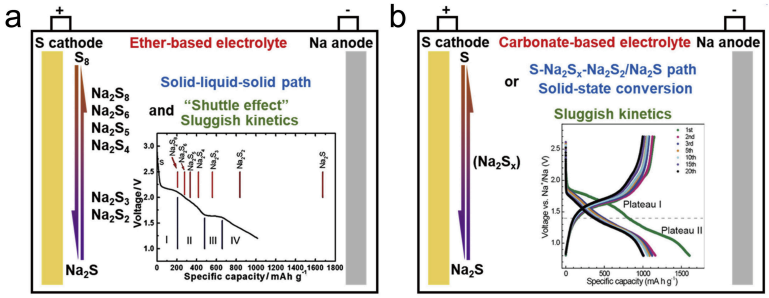


Figure 2. (**a**) Typical discharge profile of RT Na–S battery in ether-based electrolyte; (**b**) Typical discharge-charge profiles for selected cycles of RT Na–S battery in carbonate-based electrolyte. Reproduced with permission [10], Copyright 2024, Elsevier Ltd.

The first plateau, typically near 2.2 V, is associated with S_8 ring opening and formation of dissolved high-order polysulfides, represented by Equation (2).

$$S_8 + 2Na^+ + 2e^- \rightarrow Na_2S_8 \quad (2)$$

The following sloping region (approximately 2.20–1.65 V) reflects solution-phase reduction and redistribution among high- and intermediate-order polysulfides. Equation (3) provides a balanced limiting representation for conversion of Na_2S_8 to Na_2S_4; Na_2S_6 and Na_2S_5 may also be transiently populated.

$$Na_2S_8 + 2Na^+ + 2e^- \rightarrow 2Na_2S_4 \quad (3)$$

The lower-voltage plateau is associated with precipitation of short-chain species and Na_2S. Equations (4)–(6) show representative balanced branches from Na_2S_4 to Na_2S_3, Na_2S_2, or Na_2S. Their relative contributions vary with solvent donor strength, salt concentration, host chemistry, and overpotential.

$$3Na_2S_4 + 2Na^+ + 2e^- \rightarrow 4Na_2S_3 \quad (4)$$

$$Na_2S_4 + 2Na^+ + 2e^- \rightarrow 2Na_2S_2 \quad (5)$$

$$Na_2S_4 + 6Na^+ + 6e^- \rightarrow 4Na_2S \quad (6)$$

The final sloping region corresponds primarily to solid-state or interfacial conversion of Na_2S_2 to Na_2S, as represented by Equation (7). This step is often kinetically limiting

because both products are electronically insulating and because precipitation can passivate catalytic and conductive surfaces.

$$Na_2S_2 + 2Na^+ + 2e^- \rightarrow 2Na_2S \quad (7)$$

In carbonate-based electrolytes, sulfur chemistry cannot be described by simply transferring the ether-based shuttle mechanism (Figure 2b). High-order Na_2S_n species are nucleophilic and may react with carbonate solvents, while nanoconfinement and an evolving cathode–electrolyte interphase (CEI) can reduce their effective activity and promote quasi-solid or spatially localized conversion [12]. Thus, carbonate media often suppress long-range polysulfide transport kinetically rather than eliminating polysulfide formation thermodynamically. Partial dissolution, short-lived soluble intermediates, and CEI rupture remain possible, particularly during early activation, at high sulfur loading, or when the carbon host is insufficiently confining. The monotonically sloping voltage profile and lower operating voltage commonly observed in carbonate systems therefore reflect a coupled response of sulfur speciation, solvent decomposition, CEI formation, and solid-state transport—not definitive proof of a completely shuttle-free mechanism. This distinction reconciles reports of reduced shuttle with evidence for residual dissolution and interfacial instability.

2.2. Technical Challenges

RT Na–S batteries face mutually reinforcing limitations at the molecular, electrode, and cell levels. While these issues resemble those encountered in Li-S batteries, their severity is notably greater in the Na–S system. Key challenges include: (i) the inherently low electronic conductivity of sulfur (~10^{-30} S cm^{-1}), which restricts its electrochemical activity in liquid electrolytes; (ii) structural degradation of the sulfur electrode due to the formation of Na_2S_n during cycling, disrupting electronic pathways between particles; and (iii) progressive impedance growth caused by electrode passivation [13–15]. Compared with Li-S systems, these challenges are exacerbated in Na–S batteries, where sluggish redox kinetics and enhanced polysulfide diffusion combine to make performance improvements particularly difficult.

2.2.1. Shuttle Mechanism

In ether-based electrolytes, long-chain Na_2S_n (typically $4 \leq n \leq 8$) are thermodynamically soluble and can diffuse across the separator [16,17]. Their chemical reduction at the Na surface and subsequent return to the cathode establish a parasitic redox shuttle, lowering Coulombic efficiency and depleting both sulfur and Na inventory [18,19]. In carbonate electrolytes, by contrast, apparent shuttle suppression may arise from rapid solvent-derived CEI formation, low free-solvent activity, nanoconfinement, or conversion to less-soluble species. These mechanisms are kinetic and interfacial: they can immobilize polysulfides over experimental timescales without proving zero equilibrium solubility. Accordingly, polysulfide control should be discussed through three separate descriptors—thermodynamic solubility, kinetic transport across the separator, and interfacial conversion/immobilization—rather than through a binary 'shuttle/no-shuttle' classification. Although this shuttle effect is also observed in Li-S batteries, the stronger nucleophilicity of sodium widens the kinetic differences, making the shuttle more aggressive in room-temperature Na–S cells. This leads to rapid Coulombic efficiency loss and accelerated capacity fade.

2.2.2. Self-Discharge

Self-discharge represents a critical bottleneck for the practical deployment of room-temperature Na–S batteries. Under open-circuit conditions, soluble high-order polysulfides

migrate along concentration gradients toward the Na anode, where they undergo spontaneous chemical reduction, leading to irreversible depletion of active species and progressive capacity fading [20,21]. While quasi-solid carbonate and solid-state electrolytes can effectively mitigate long-range polysulfide diffusion, parasitic processes—including local redox redistribution, interphase degradation, mixed ionic-electronic conduction, and direct chemical interactions—continue to drive state-of-charge decay. Consequently, rigorous evaluation of self-discharge requires standardized conditions encompassing temperature, rest duration, sulfur loading, and electrolyte composition.

2.2.3. Electronic/Ionic Transport and Electrode Passivation

Sulfur and Na_2S possess extremely low electronic conductivity, so conversion proceeds only where ion-conducting electrolytes, electronic pathways, and active sulfur remain in contact. At high loading, tortuous diffusion through thick cathodes produces reaction fronts, local salt depletion, and nonuniform Na_2S deposition. Precipitated products can block pores and catalytic sites, while repeated solvent decomposition increases interfacial resistance. High surface area is therefore not intrinsically beneficial: it improves reaction area but can increase electrolyte demand, side reactions, and inactive interphase mass. Practical hosts must preserve continuous electronic percolation while maintaining short Na^+ transport distances and controlled electrolyte accessibility.

2.2.4. Structural Evolution and Mechanical Degradation

Conversion between S_8 and Na_2S is accompanied by substantial local volume redistribution. In thin electrodes, free pore volume can mask this problem; in high-loading electrodes, however, repeated precipitation and dissolution generate stress gradients, particle detachment, binder fatigue, pore closure, and current-collector delamination. Loss of conductive contact promotes isolated sulfur/Na_2S domains and accelerates impedance growth. Mechanical robustness, pore-size hierarchy, binder chemistry, and electrode density must therefore be optimized together rather than treated as secondary processing variables.

2.2.5. Na-Metal Instability and Safety

The Na-metal anode experiences nonuniform plating, dendrite formation, polysulfide corrosion, and repeated SEI fracture. Excess Na can conceal these losses in coin cells but lowers cell-level energy density and delays rather than resolves failure. Reactive sodium also amplifies safety risks associated with electrolyte leakage, gas evolution, internal short circuit, and heat generation. A credible practical assessment must therefore report Na thickness or N/P ratio, cumulative plated capacity, full-cell inventory balance, and abuse-relevant safety data.

3. Recent Advances in RT Na–S Batteries

Recent advances can be grouped into four coupled design layers: (i) cathode architectures that maintain electronic/ionic percolation and regulate sulfur speciation; (ii) catalytic motifs that lower barriers for Na_2S_n interconversion and Na_2S nucleation/decomposition; (iii) Na-anode interphases that homogenize ion flux and suppress corrosion; and (iv) electrolyte/solid-electrolyte chemistries that control solvation, interphase formation, and transport. Because improvements in one layer can shift failure to another, performance should be compared under matched loading, E/S ratio, Na inventory, and cell format (Table 1).

Table 1. Quantitative comparison of representative RT Na–S strategies.

No.	Cathode or Strategy	Sulfur Loading	E/S Ratio	Current Density/Rate	Cycling Stability	Coulombic Efficiency	N/P Ratio	Cell Configuration/Electrolyte
[22]	Heterointerfaced nanoreactor electrocatalyst for practical RT Na–S batteries	6.2 mg cm^{-2}	9 μL mg^{-1}	0.1 C	1300 mAh g^{-1} over 100 cycles	Near 100% reported in consulted source	Not reported	Na‖S coin and pouch cells; nanoreactor-confined catalytic sulfur cathode
[23]	Binder-free S@Fe_3N-NMCN electrocatalytic cathode	~2.6 mg cm^{-2}	18.2 μL mg^{-1}	long cycling at 8375 mA g^{-1}	almost no attenuation after 2800 cycles at 8375 mA g^{-1};	Initial CE 92%; near-100% CE during long cycling	Not reported	CR2032 Na‖S coin cell; glass-fiber separator; 1 M NaPF6 in DOL/DIGLYME (1:1); RT
[24]	$MoTe_2$ nanosheets vertically grown on graphene coupled with sulfur (MTG/S)	3.5 mg cm^{-2}	7 μL mg^{-1}	0.1 C for high-loading cycling	1081 mAh g^{-1} initial at 0.1 C; 901 mAh g^{-1} after 350 cycles at 0.1 C	~100% over 350 cycles; capacity decay ~0.05% per cycle	Not reported	Na‖MTG/S coin cell; localized high-concentration electrolyte (NaFSI/DME/TTE); RT
[25]	Solvation inner-sheath engineering/non-coordinating co-solvent electrolyte for practical Na–S cells	1.8 mg cm^{-2}	18 μL mg^{-1}	0.1 C	530 mAh g^{-1} over 200 cycles	Not reported	Not reported	Na‖S pouch/practical-format cells; lean electrolyte; non-coordinating co-solvent electrolyte design

Table 1. *Cont.*

No.	Cathode or Strategy	Sulfur Loading	E/S Ratio	Current Density/Rate	Cycling Stability	Coulombic Efficiency	N/P Ratio	Cell Configuration/Electrolyte
[26]	Free-standing carbon@sulfur framework with NLP-selected single-atom Co-N/S catalyst	Pouch: 4.5 mg cm^{-2}; stricter pouch: 6.67 mg cm^{-2}; high-loading coin: 4.2 mg cm^{-2}	8 µL mg^{-1} for 4.5 mg cm^{-2} pouch; 3.2 µL mg^{-1} for 6.67 mg cm^{-2} pouch	Pouch rate tests at 0.1–1.0 A g^{-1}; 4.5 mg cm^{-2} pouch tested under 2 mA	4.5 mg cm^{-2} pouch: 173.9 Wh kg^{-1} after 10 cycles; 6.67 mg cm^{-2} pouch: 173 mAh first cycle; high-loading coin: 2.54 mAh cm^{-2} after 70 cycles	Close to 100% for 4.2 mg cm^{-2} coin cell after 70 cycles	3.4:1 for 4.5 mg cm^{-2} pouch; 2.1:1 for 6.67 mg cm^{-2} pouch	Na‖S pouch cells with thin Na slice; 2 M NaTFSI in PC/FEC; glass-fiber separator
[27]	Ca-O_4N-C@S s-block single-atom catalyst with axial-ligand-induced charge localization	1.0 mg cm^{-2}; 3.78 mg cm^{-2} high-loading test also reported	70 µL mg^{-1}	335 mA g^{-1} (0.2 C); 3 C long cycling	1.0 mg cm^{-2} coin: 1211 mAh g^{-1} after 100 cycles at 0.2 C; 887 mAh g^{-1} after 800 cycles at 3 C; 3.78 mg cm^{-2} coin: 978 mAh g^{-1} at 0.2 C after 100 cycles	Pouch: 99.50% after 50 cycles at 0.1 C	Not reported	CR2032 Na‖S; GF/D separator; 2 M NaTFSI in PC/FEC (1:1); 0.5–2.8 V

Mechanistic assignment increasingly relies on complementary operando methods. Operando Raman spectroscopy and synchrotron X-ray diffraction have directly followed sulfur-species evolution and phase formation in catalytic RT Na–S cells [28]. More recently, operando transmission X-ray microscopy combined with sulfur K-edge X-ray absorption spectroscopy resolved spatially heterogeneous sulfur conversion, cathode expansion, and active-material dissolution in an ether electrolyte [29], while operando microbeam XRD, XPS, and ex situ XAS exposed pressure-dependent polysulfide formation in solid-state cells. These studies illustrate why ex situ end-point characterization alone can misidentify transient intermediates or overlook reaction heterogeneity.

3.1. Cathode: From Host Design to Catalytic Mechanism Innovation

Cathode-host engineering remains the most direct and widely explored approach for mitigating polysulfide shuttling. Conventional strategies based on physical adsorption in porous carbon matrices rely on weak, non-selective van der Waals interactions; under high sulfur loading and lean-electrolyte conditions, however, pore saturation occurs, and polysulfide shuttling continues largely unchecked [30]. Yet pore architecture also imposes fundamental trade-offs. Micropores strengthen confinement and favour short-chain or quasi-solid conversion, but restrict sulfur loading and electrolyte infiltration; mesopores shorten ion-transport paths and accommodate products, but can permit polysulfide escape; macropores improve wetting and buffer volume change, but lower volumetric energy density. A hierarchical pore network is therefore preferable only when pore volume, sulfur distribution, tortuosity, and electrolyte inventory are co-optimized. Furthermore, the non-polar surfaces of pristine carbon materials exhibit limited electronic coupling with polar polysulfides, resulting in sluggish conversion kinetics.

Conductive additives must form a continuous network through the full electrode thickness, while binders must sustain adhesion during repeated conversion. Recent SPAN studies show that poly(acrylic acid) can outperform conventional PVDF by hydrogen-bonding with polar C=N motifs, distributing stress more uniformly and sustaining an areal capacity of 2.6 mAh cm^{-2} for more than 200 cycles [31]. This example underscores that binder chemistry, slurry rheology, calendering density, and current-collector adhesion can determine whether a catalytic material remains accessible under practical loading.

Defect engineering and heteroatom coordination modify the local electronic density of states and thereby tune the adsorption–conversion balance for Na_2S_n. Pentagon defects disrupt the π-conjugated carbon lattice, localize charge, and lower barriers for S–S bond cleavage, as shown in Figure 3a; Zheng et al. reported 1275 mAh g^{-1} after 100 cycles at 0.1 C and a decay rate of 0.035% per cycle over 600 cycles at 3 C, as shown in Figure 3b [32]. The mechanistic objective is not maximal adsorption: excessively strong binding can immobilize intermediates and retard product desorption. Effective hosts instead approach a Sabatier-type optimum in which adsorption suppresses escape while allowing rapid interconversion and Na_2S release.

Wei et al. integrated catalytic sites and spatial confinement in a heterointerfaced nanoreactor [22]. Interfacial electronic coupling shifts the transition-metal d-band centre, strengthens selective chemisorption, and accelerates reduction, while the surrounding carbon shell limits species loss and accommodates expansion, as shown in Figure 3c. Importantly, the system was also evaluated at 6.2 mg cm^{-2} sulfur loading and an E/S ratio of 9 μL mg^{-1}, and in a pouch-cell configuration. Although this remains above the stringent E/S ≤ 5 μL mg^{-1} benchmark adopted here, it represents a more informative practical test than conventional low-loading coin cells.

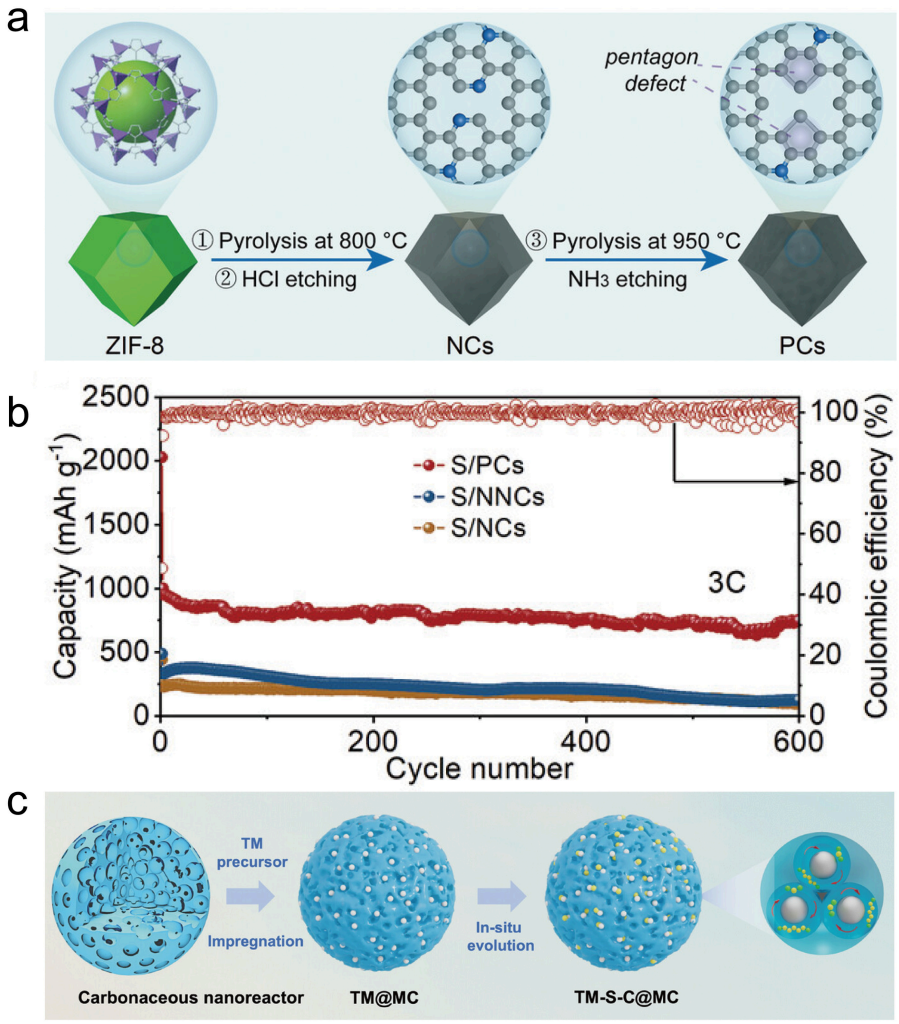


Figure 3. (**a**) Schematic illustration of the synthesis process for PCs; (**b**) Long-term cycling stability of S/PCs, S/NNCs and S/NCs at 3 C. The red hollow circle represent the Coulombic efficiency. Reproduced with permission [32], Copyright 2024, Wiley-VCH; (**c**) Schematic illustration of TM-S-C@MC structure and its sulfur reduction reaction catalytic process. Reproduced with permission [22], Copyright 2025, Wiley-VCH.

The quintessential challenge in cathode design lies in simultaneously suppressing polysulfide dissolution/shuttling and accelerating sulfur redox kinetics. Zhang et al. [33] promoted a quasi-solid-state conversion pathway by embedding MoC-W_2C heterostructures within multichannel carbon nanofibers. This hetero-interface facilitates rapid electron/ion transport, enabling the electrode to retain a capacity of 200 mAh g^{-1} after 3500 cycles at 4 Ag^{-1}. In parallel, Li et al. [34] engineered an asymmetric Mn-N_2 coordination motif that intensifies d-p orbital hybridization, which elevated the catalytic turnover of polysulfides, resulting in a retained capacity of 458 mAh g^{-1} after 2300 cycles at 3 C. More strikingly, Li et al. [35] developed a Fe–Co dual-atom catalyst in which Fe incorporation switches Co(II) from a low-spin to a high-spin state, markedly accelerating sodium polysulfide interconversion (Figure 4a,b). The Fe–Co/NC/S electrode exhibits a voltage gap of merely 0.87 V between the second cathodic and anodic peaks—significantly lower than those of Co/NC (0.92 V) and Fe/NC (1.04 V) counterparts—indicating substantially reduced polarization (Figure 4c). Fe–Co dual-atom sites altered the Co spin state and reduced polarization; high-loading cells containing 5.6 mg cm^{-2} sulfur were also demonstrated. Figure 4d further confirms a discharge capacity of 341.1 mAh g^{-1} at 5 A g^{-1}. Collectively, these studies underscore that electronic-structure modulation and interfacial engineering can funda-

mentally alter polysulfide reaction pathways. Extending this paradigm, Gao et al. [36] constructed a heterostructured Na_2S/Na_2Te@C cathode mediated by a sodium thiotellurate (Na_2TeS_3) interphase. The abundant electron/ion channels within this architecture enhance active-material utilization while curbing polysulfide shuttling (Figure 4e), enabling an initial discharge capacity of 634 mAh g^{-1} in an anode-free configuration. Nevertheless, the majority of these advances remain confined to laboratory-scale evaluations under low sulfur loadings. Their operative mechanisms under practical conditions such as high sulfur mass loading and lean electrolyte—await systematic elucidation.

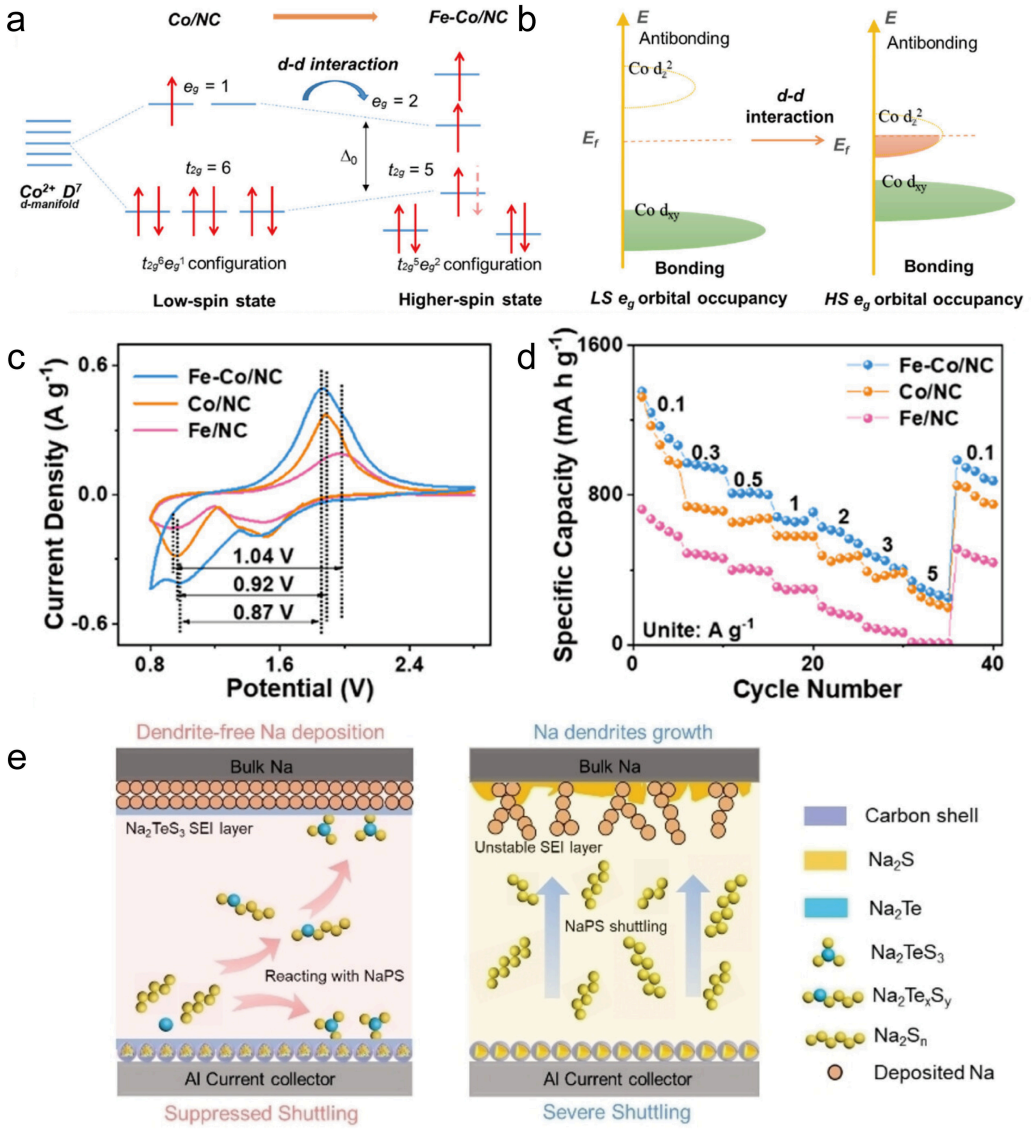


Figure 4. (**a**,**b**) Spin-state modulation and d–d interaction in Co/NC and Fe–Co/NC; (**c**) cyclic-voltammetry comparison and (**d**) rate performance of Fe–Co/NC/S, Co/NC/S, and Fe/NC/S cathodes. Reproduced with permission [35], Copyright 2025, American Chemical Society; (**e**) Schematic mechanism for enhancing the electrochemical performance of Na_2S/Na_2Te@C in RT Na–S batteries. Reproduced with permission [36], Copyright 2024, Wiley-VCH.

Dynamic active-site reconstruction must nevertheless be considered: electrochemically generated Mo single atoms on MoS_2, for example, can become the true catalytic centres rather than the pristine phase identified before cycling [37]. Operando spectroscopy, post-mortem mass balance, and matched-loading controls are therefore required to establish causal structure–activity relationships.

3.2. Anode: Interface Engineering and Deposition Behaviour Regulation

The metallic sodium anode confronts a bifurcated challenge—dendrite growth and parasitic interfacial reactions—both of which are intensified by the polysulfide-rich environment. To address this challenge, Liu et al. [38] used a nonflammable ionic-liquid electrolyte containing $FSI^-/TFSI^-$ anions and FEC to generate an inorganic-rich, F-containing inorganic-rich solid-electrolyte interphase (SEI) on Na surface, which promotes uniform sodium deposition and suppresses dendrite propagation (Figure 5a). Leveraging the synergistic effect of $FSI^-/TFSI^-$ anions and fluoroethylene carbonate (FEC), the electrolyte enables a capacity retention of 565 mAh g^{-1} after 500 cycles at 0.2 A g^{-1} (Figure 5b,c). By contrast, Wang et al. [39] introduced tin trifluoromethanesulfonate ($Sn(OTf)_2$) into a non-flammable phosphate-based electrolyte. By modifying the Na^+ solvation sheath and interfacial chemistry, the additive facilitates the formation of Na–Sn-alloy-containing SEI together with a cathodic CEI layers, which increase the cell capacity from 322 to 906 mAh g^{-1} (Figure 5d). The resulting Na–S full cell also demonstrates superior rate capability, further confirming the significant electrochemical improvement imparted by $Sn(OTf)_2$ (Figure 5e).

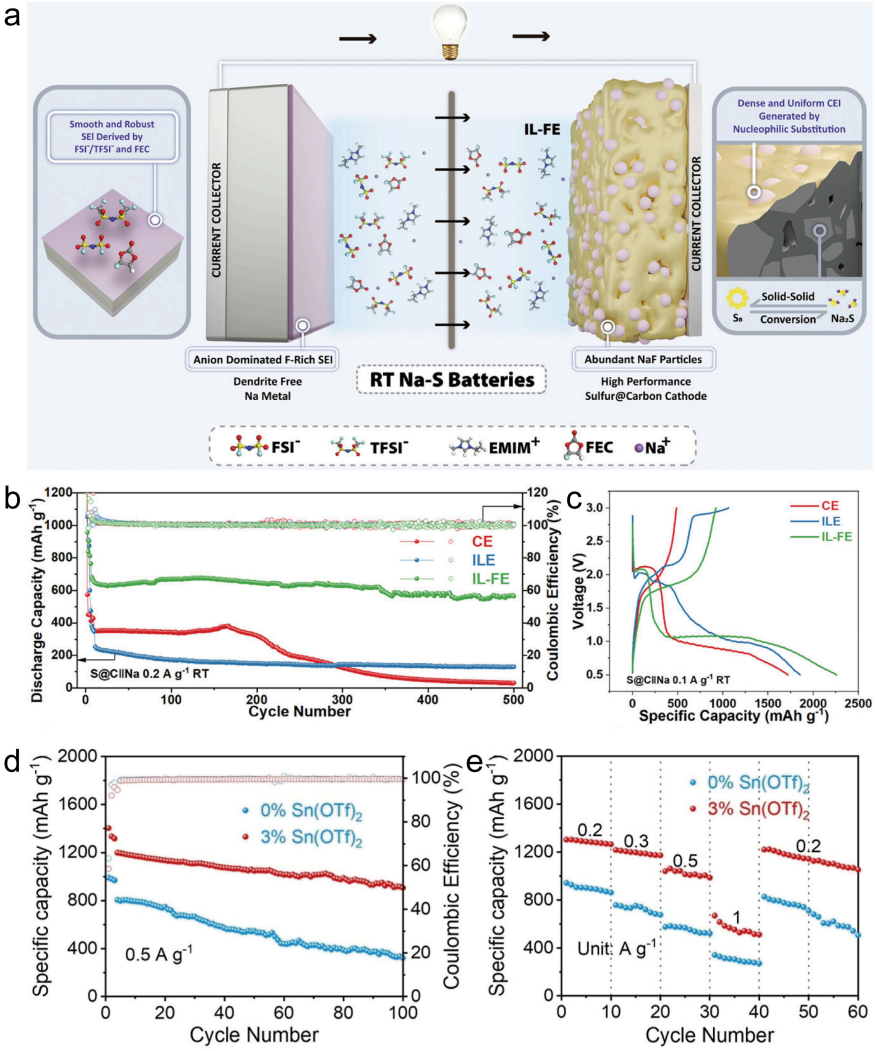


Figure 5. (**a**) Schematic diagram of S@C||Na cell with the IL-FE electrolyte. (**b**) Cycle performance at 0.2A g^{-1}. (**c**) Initial charge–discharge profiles at 0.2A g^{-1}. Reproduced with permission [38], Copyright 2025, WILEY-VCH. (**d**) Cycling performance at 0.5A g^{-1} and (**e**) rate performance of Na–S full cells using the electrolyte with and without Sn $(OTf)_2$ additive. The red hollow circle represent the Coulombic efficiency. Reproduced with permission [39], Copyright 2024, WILEY-VCH.

These interphases should be compared by composition, transport, and mechanics rather than by the generic label 'stable SEI/CEI'. NaF-rich layers offer high interfacial energy and mechanical stiffness but can become resistive if excessively thick; alloy-containing SEIs can improve sodiophilicity and lateral Na diffusion but consume additive and active Na; organic-rich components can enhance elasticity yet remain susceptible to nucleophilic attack. Long-term validation therefore requires impedance evolution, Na Coulombic efficiency, gas analysis, and morphology after a fixed cumulative areal capacity—not only short symmetric-cell tests.

Beyond additive-based approaches, interphase design can be advanced through solvent engineering. Weng et al. [40] revealed a two-stage CEI formation mechanism when FEC is used as the sole solvent (Figure 6a): rapid nucleophilic attack combined with electrochemical cleavage produces a distinctive "chocolate-biscuit" bilayer CEI rich in NaF. Coupled with a fluorine-enriched SEI on the anode, the FEC-only S@MRP||Na full cell outperformed its PCE-containing counterpart across rates from 0.1 C to 2 C (Figure 6b) and retained 456 mAh g^{-1} after 1000 cycles at 0.5 C, with Coulombic efficiency approaching unity (Figure 6c). These results highlight that constructing an interphase with high ionic conductivity and mechanical robustness is crucial for dendrite suppression. However, most current studies are still based on half-cell evaluations. Stabilizing Na-metal anodes in full-cell configurations under practical conditions—such as low N/P ratio and lean electrolyte—remains a significant challenge.

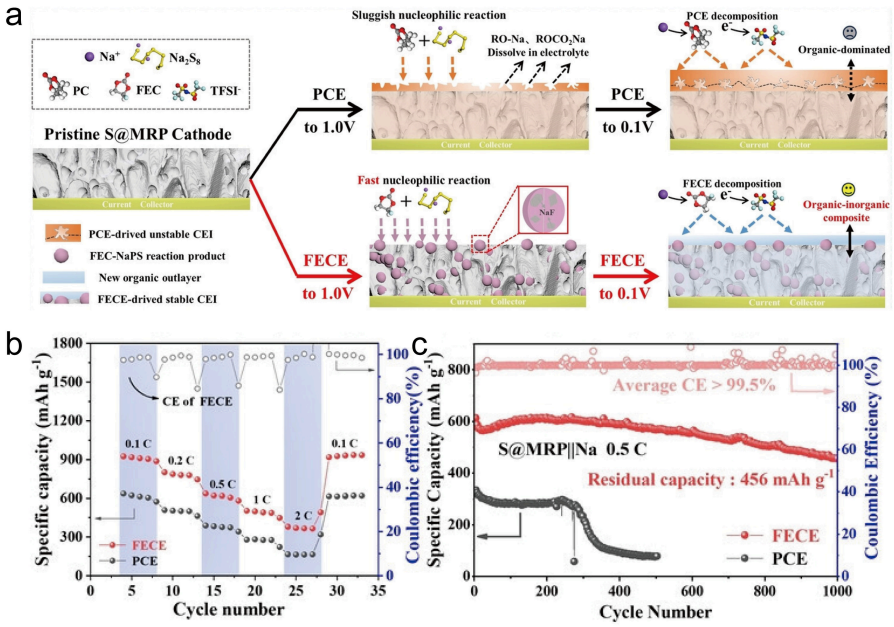


Figure 6. (**a**) Schematic diagram of complete CEI formation mechanism in S@MRP||Na cells with two electrolytes. (**b**) Rate capability. (**c**) Long-cycle performance at 0.5 C. The red hollow circle represent the Coulombic efficiency. Reproduced with permission [40], Copyright 2025, WILEY-VCH.

3.3. Electrolyte: Precise Design from Solvation Structure to Interfacial Chemistry

The electrolyte is simultaneously an ion-transport medium, a solvent for sulfur species, and a precursor to SEI/CEI formation. Its effect cannot be reduced to polysulfide solubility alone. Donor strength and salt association determine equilibrium speciation; viscosity and conductivity control kinetic transport; preferential interfacial decomposition determines whether dissolved species are immobilized or whether fresh surfaces remain exposed. Electrolyte design must therefore balance thermodynamic solubility, kinetic shuttle suppression, interfacial passivation, Na plating efficiency, wetting of thick electrodes, and safety.

Pai et al. [41] innovatively employed toluene—a non-fluorinated, low-cost diluent—to construct a localized high-concentration electrolyte (LHCE). Toluene not only provides reductive stability but also modulates the solvation structure, promoting anion-dominated clusters that foster a dense, inorganic-rich SEI on the Na metal surface (Figure 7a). This interphase effectively suppresses dendrite growth and minimizes parasitic electrolyte–anode interactions. As shown in Figure 7b, polysulfide attack leads to rugged dendrites in 2 M-DME electrolytes, whereas the LHCE-cycled electrode retains a smooth, planar morphology. The approach trades some solvation capacity for enhanced interfacial stability, simultaneously mitigating polysulfide shuttle and dendrite formation. Extending this paradigm, Yao et al. [42] systematically investigated solvent molecular frameworks, revealing a decisive link between solvation structure and electric-double-layer (EDL) chemistry. An LHCE formulated with tetrahydropyran (THP) not only reduces polysulfide solubility through solvation restructuring but also promotes a durable inorganic SEI, enabling stable cycling over 500 cycles at 1.0 C with a minimal capacity fade rate of 0.07% per cycle (Figure 7c). These results show that bulk solvation and interfacial composition must be designed together.

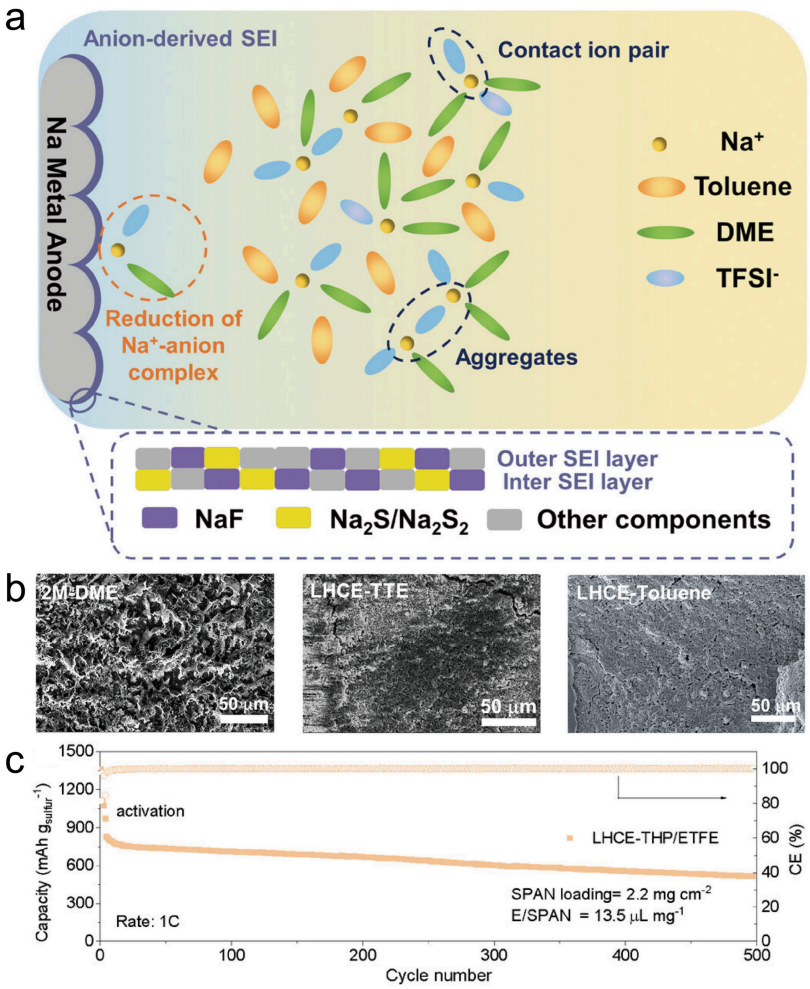


Figure 7. (**a**) Schematic illustration of the electrolyte solvation structure with a non-fluorinated diluent, toluene; (**b**) SEM images of sodium metal from the Na||Na symmetric cells after cycling for 300 h. Reproduced with permission [41], Copyright 2024, WILEY-VCH; (**c**) Long-cycle performances of Na–S cells with LHCE-THP/ETFE electrolyte at 1 C rate. The orange hollow circle represent the Coulombic efficiency. Reproduced with permission [42], Copyright 2025, WILEY-VCH.

In a subsequent study, Yao et al. [43] proposed an "inner–outer sheath synergistic shielding" strategy. By employing sterically hindered 1, 2-dimethoxypropane (DMP) as the

inner-shell solvent, the additional methyl group effectively excludes polysulfides from the primary solvation sheath (Figure 8a). Complementarily, a fluorinated ether (TFTFE) with low solvation power serves as the outer diluent, further suppressing polysulfide dissolution. This dual-sheath design offers a new perspective for inhibiting the shuttle effect at its origin. Parallel to this, Zou et al. [44] developed a weakly solvating anion-stabilized (WSAS) electrolyte that re-balances Na^+-solvent and Na^+-anion interactions, generating abundant contact ion pairs (CIPs) and aggregates (AGGs). The resulting electrolyte supports a 4.0 V-class layered-oxide cathode across a wide temperature range (−40 °C to 60 °C), and achieves an average Na plating/stripping Coulombic efficiency of 99.89% (Figure 8b). These advances highlight the progression of electrolyte design from simple component selection toward precise solvation-structure engineering. Such LHCEs, however, carry nontrivial penalties: concentrated salts and fluorinated diluents increase cost and environmental burden; viscosity can impair wetting and low-temperature transport; reduced ionic conductivity increases polarization in thick electrodes; and limited free solvent can hinder complete utilization at high sulfur loading. Developing cost-effective and recyclability yet inherently safe formulations thus remains crucial for commercial adoption.

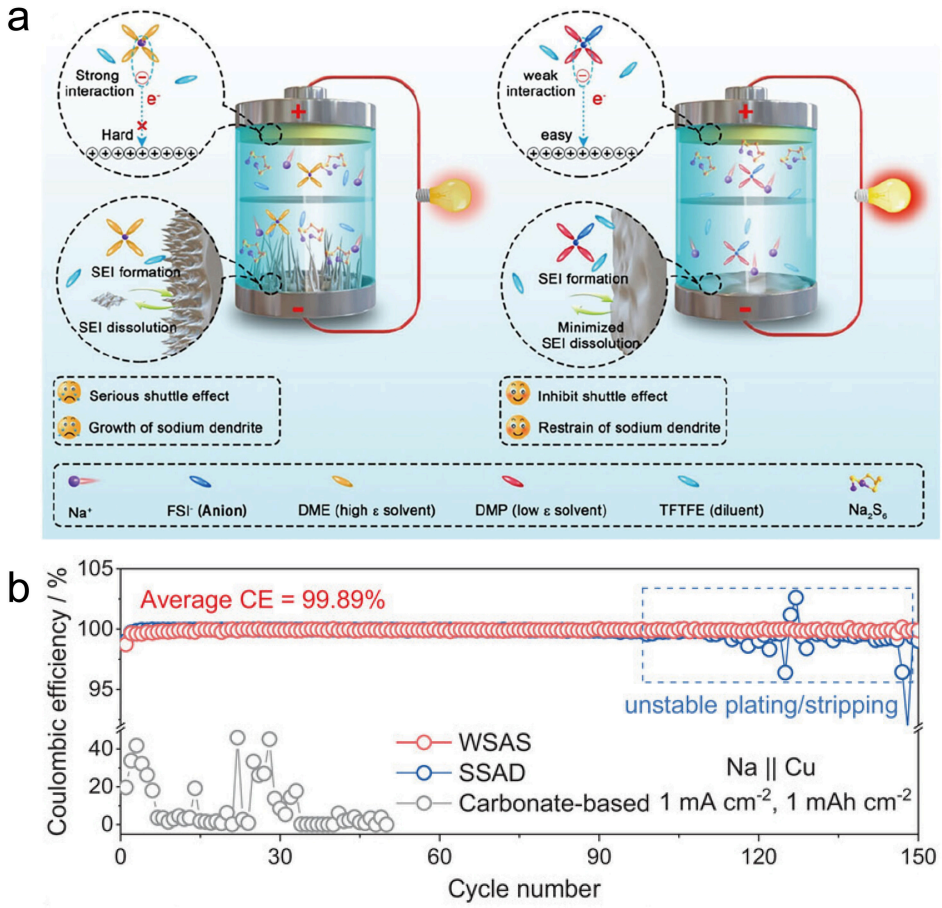


Figure 8. (**a**) Schematic diagram of Na–S batteries through different LHCE. Reproduced with permission [43], Copyright 2025, American Chemical Society; (**b**) Na plating/stripping Columbic efficiency (CE) of cycling performance in Na||Cu asymmetric cells at 1.0 mA cm^{-2}. Reproduced with permission [44], Copyright 2024, WILEY-VCH.

3.4. All-Solid-State Na–S Batteries: Suppressed Long-Range Shuttle, Persistent Interfacial Chemistry

All-solid-state Na–S batteries replace liquid-mediated long-range polysulfide transport with solid–solid or locally confined conversion. This architecture can suppress macroscopic

dissolution and separator-crossing shuttle, but it does not eliminate sulfur intermediates, interfacial side reactions, or chemo-mechanical failure. Sulfide electrolytes provide high Na^+ conductivity and intimate chemical affinity with sulfur, yet they are moisture-sensitive and can undergo redox decomposition; borohydride or halide-containing conductors may offer wider stability windows but introduce processing, pressure, or cost constraints. In all cases, reaction kinetics depend on a percolating three-phase network of active sulfur, ionic conductor, and electronic conductor.

Recent research has shifted toward all-solid-state Na–S batteries, based on the premise that solid electrolytes can effectively suppress the long-range dissolution and diffusion of polysulfides that characterize liquid electrolyte systems. However, this does not imply that sulfur intermediate formation or interfacial side reactions are entirely eliminated. Nguyen et al. [45] detected "clandestine polysulfides" in solid-state cells via operando scanning microbeam XRD, operando XPS, and ex situ XAS (Figure 9a). Within Na_3PS_4-type electrolytes, they identified various crystalline and amorphous polysulfides—including Na_2S_3 phases previously stabilized only under elevated temperature and pressure—that persist throughout cycling (Figure 9b). This finding challenges the conventional understanding of interfacial chemistry in solid-state batteries, demonstrating that sulfur conversion pathways persist even without liquid media, albeit constrained by local stress, interfacial contact, and ionic percolation. Moreover, their results also demonstrate that applied pressure is both a thermodynamic variable and a transport parameter: insufficient pressure causes contact loss and ionic isolation, whereas excessive pressure can alter phase selection, densify pathways, and aggravate local stress. In essence, while solid electrolytes act as physical barriers, they cannot prevent interfacial complications arising from sulfur-redox intermediates.

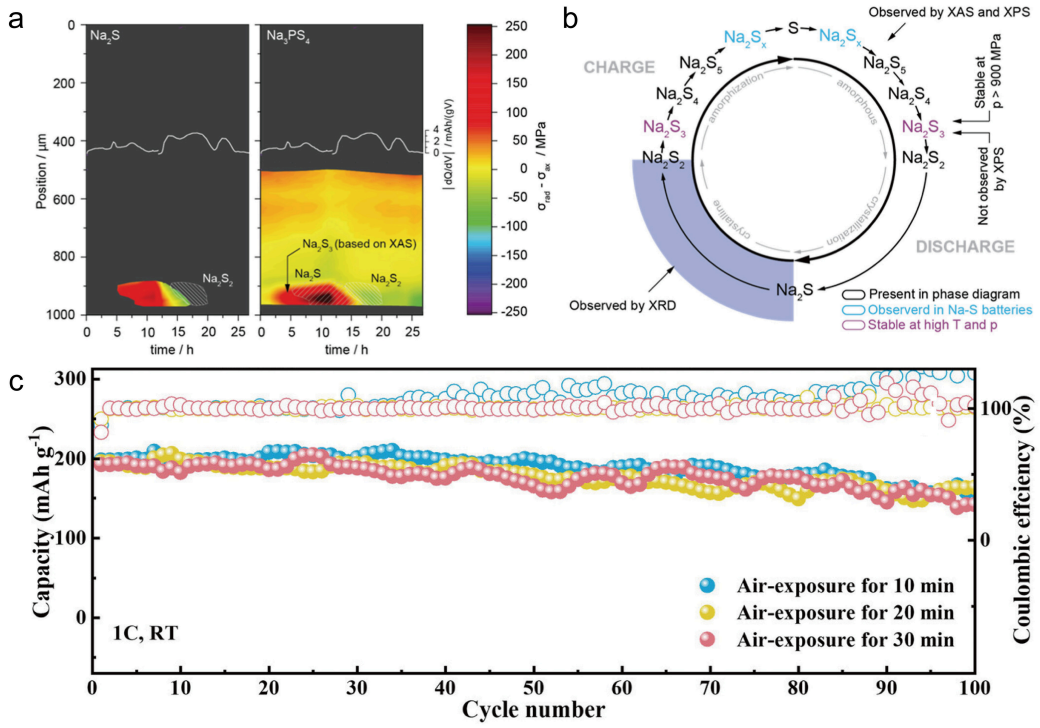


Figure 9. (**a**) Time-dependent evolution of stress profiles across the cross-section of the cell during charge and discharge; (**b**) Summary of reaction pathway during charge and discharge. Reproduced with permission [45], Copyright 2025, American Chemical Society; (**c**) Cycling performance of 5%SP-TiS_2//Na_5Sn ASSSBs at 1 C using NSS2 electrolyte exposed to 50% RH air for different times. The hollow circle represent the Coulombic efficiency. Reproduced with permission [46], Copyright 2024, WILEY-VCH.

Practical all-solid-state development must address cathode composite homogeneity, stack-pressure retention, interfacial resistance, electronic leakage, volume-change accommodation, and environmental stability during manufacturing. Addressing the moisture sensitivity of sulfide electrolytes, Guo et al. [46] designed a humid-air-tolerant $Na_{3-x}Sb_{1-4x}(SnWCaTi)_xS_4$ phase through vacancy engineering and configurational-entropy enhancement. The corresponding solid-state cell retained stable cycling for 100 cycles at 1 C after 30 min exposure to air with a dew-point of 13.8 °C (Figure 9c), underscoring that environmental stability is as critical as electrochemical performance for the practical deployment of solid-state batteries. Vacancy and entropy engineering have improved humid-air tolerance of sulfide electrolytes, but performance should be validated after realistic dry-room exposure and in cells with industrially relevant areal capacity. Operando diffraction, XAS, Raman spectroscopy, acoustic/mechanical diagnostics, and cryogenic electron microscopy will be essential for correlating phase evolution with contact loss and fracture [47].

4. Conclusions and Outlook

Substantial progress in room-temperature sodium–sulfur (RT Na–S) batteries has been enabled by catalytic host design, Na-anode interfacial regulation, and solvation engineering. Single-atom catalysts, heterostructures, and defect-rich scaffolds suppress polysulfide shuttling and accelerate sulfur redox, while SEI regulation and tailored solvation improve Na stability. However, as summarized in Table 1, many record performances rely on low sulfur loading, excess electrolyte, high Na excess, and incomplete reporting, and the operando mechanisms of polysulfide conversion and interface evolution remain insufficiently resolved. The field must therefore shift from maximizing specific capacity toward coordinated control of sulfur chemistry, transport, finite Na inventory, interfacial mechanics, and safety.

4.1. Practical Benchmarks and Failure Modes

For the purpose of cross-study evaluation, we recommend that 'practical' RT Na–S cells be screened at sulfur loadings ≥ 5 mg cm^{-2}, E/S ratios ≤ 5 µL mg^{-1}, areal capacities ≥ 4 mAh cm^{-2}, and limited Na excess (preferably N/P ≤ 3), followed by validation in pouch or otherwise externally pressurized full cells. These values are not rigid standards, but they expose failure modes that thin, flooded coin cells conceal. At high loading, electrolyte depletion and tortuous transport generate through-thickness reaction gradients; at low E/S, salt concentration and viscosity change dynamically as sulfur species form; and at low N/P, even small parasitic currents rapidly exhaust the Na inventory.

Future studies should report the complete mass and capacity balance: sulfur areal loading, sulfur fraction, electrode density and thickness, electrolyte volume, separator thickness, Na foil thickness or N/P ratio, formation protocol, stack pressure, temperature, self-discharge, and cumulative plated capacity. Capacity retention should be accompanied by Coulombic efficiency with sufficient precision, impedance evolution, and post-mortem quantification of inactive sulfur and Na. Gradient electrodes—combining high electronic conductivity near the current collector, controlled catalytic/polar functionality through the reaction zone, and mechanically compliant interfaces—offer a promising route to reconcile transport and stress at high loading.

4.2. Safety, Manufacturability, and Outlook

Safety assessment must extend beyond electrolyte flammability. Metallic Na can react vigorously with trace moisture and leaked electrolyte; internal short circuits can couple dendritic heating with exothermic interphase reactions; and solvent decomposition or polysulfide reactions can generate gas and pressure. Practical studies should therefore include accelerating-rate calorimetry or differential scanning calorimetry of charged components,

gas analysis, nail/overcharge and external-short tests where appropriate, leak and seal validation, and procedures for Na handling, module isolation, and end-of-life deactivation.

The most credible path forward is an integrated design loop linking computation, operando characterization, scalable processing, and full-cell validation. Cathode hosts must preserve percolation and mechanical integrity under lean electrolyte; electrolytes must balance solvation, conductivity, interphase chemistry, cost, and environmental impact; and Na anodes must operate with finite inventory over industrially relevant cumulative capacity. For all-solid-state cells, the priority is not simply higher ionic conductivity but stable three-phase contact under controlled pressure and ambient exposure. Only studies that align mechanistic claims with complete practical metrics can establish whether RT Na–S batteries can deliver competitive energy density, long life, and inherent safety.

Author Contributions: Z.S.: investigation, writing—original draft, formal analysis. Z.S. and S.T. contributed equally to this study. X.Y.: resources, formal analysis, visualization. Q.W.: formal analysis, software. J.C.: visualization. D.Z.: visualization, software. C.D.: writing—review & editing, methodology, visualization, supervision. Y.D.: supervision, and writing review & editing, funding acquisition. X.L.: writing—review & editing, visualization, funding acquisition. All authors have read and agreed to the published version of the manuscript.

Funding: The work described in this paper was supported by CHN Energy Investment Group (GJNY-25-104) and Hainan Province Postdoctoral Research Funding Project (2025-154).

Data Availability Statement: The original contributions presented in this study are included in the article. Further inquiries can be directed to the corresponding authors.

Conflicts of Interest: Authors Xuechao Yang, Qi Wang and Jia Chang were employed by the company CHN Energy Yulin Chemical Co., Ltd. The remaining authors declare that the research was conducted in the absence of any commercial or financial relationships that could be construed as a potential conflict of interest.

Nomenclature

The following abbreviations, notations, parameter symbols, and units are used in this review.

Category	Abbreviation or Notation	Definition
General	RT Na–S	Room-temperature sodium-sulfur battery
General	ASSSBs	All-solid-state sodium-sulfur batteries.
Interphase	SEI	Solid-electrolyte interphase
Interphase	CEI	Cathode-electrolyte interphase.
Electrolyte	LHCE	Localized high-concentration electrolyte.
Metric	CE	Coulombic efficiency
Material	SPAN	Sulfurized polyacrylonitrile.
Material	PVDF	Poly(vinylidene fluoride), a conventional electrode binder.
Method	SEM	Scanning electron microscopy.
Method	XRD	X-ray diffraction.
Method	XPS	X-ray photoelectron spectroscopy.
Method	XAS	X-ray absorption spectroscopy.
Electrolyte	DOL	1,3-Dioxolane.
Electrolyte	DIGLYME	Diethylene glycol dimethyl ether (bis(2-methoxyethyl) ether).
Electrolyte	DME	1,2-Dimethoxyethane.
Electrolyte	DMP	1,2-Dimethoxypropane.

Electrolyte	THP	Tetrahydropyran.
Electrolyte	ETFE	Ethyl 1,1,2,2-tetrafluoroethyl ether
Electrolyte	TFTFE	1,1,2,2-Tetrafluoroethyl 2,2,2-trifluoroethyl ether, used as an outer-sheath diluent.
Electrolyte	PC	Propylene carbonate.
Electrolyte	FEC	Fluoroethylene carbonate.
Electrolyte	FSI^-	Bis(fluorosulfonyl)imide anion.
Electrolyte	$TFSI^-$	Bis(trifluoromethanesulfonyl)imide anion.
Electrolyte	$NaPF_6$	Sodium hexafluorophosphate.
Electrolyte	NaFSI	Sodium bis(fluorosulfonyl)imide.
Electrolyte	NaTFSI	Sodium bis(trifluoromethanesulfonyl)imide.
Electrolyte	$Sn(OTf)_2$	Tin(II) trifluoromethanesulfonate.
Cell	CR2032	20 mm diameter, 3.2 mm height coin-cell format.
Cell	GF/D	Grade GF/D glass-microfiber separator.
Cell	Na||Na	Symmetric sodium-metal cell.
Cell	Na||Cu	Asymmetric sodium-copper cell for sodium plating/stripping evaluation.
Material	S@C	Sulfur hosted in or supported on carbon.
Material	MoC-W_2C	Molybdenum carbide-tungsten carbide heterostructure.
Material	Fe–Co/NC/S	Sulfur cathode with Fe–Co dual-atom sites on N-doped carbon.
Material	Co/NC/S	Sulfur cathode with Co sites on N-doped carbon.
Material	Fe/NC/S	Sulfur cathode with Fe sites on N-doped carbon.
Material	Na_2S/Na_2Te@C	Carbon-supported Na_2S/Na_2Te heterostructured cathode.
Material	Na_2TeS_3	Sodium thiotellurate interphase.
Material	SP	Super P conductive carbon
Material	SP-TiS_2//Na_5Sn	All-solid-state cell using an SP-TiS_2 composite cathode and a Na_5Sn alloy anode.
Species	Na	Sodium metal
Species	S	Sulfur active material
Species	S_8	Cyclooctasulfur, the molecular form of elemental sulfur used in the reaction scheme.
Species	Na_2S_n	Sodium polysulfide with chain-length index n. The review discusses $n = 2$–8, with long chains typically $4 \leq n \leq 8$.
Species	$Na_2S_8/Na_2S_6/Na_2S_5/Na_2S_4/Na_2S_3/Na_2S_2/Na_2S$	Representative sodium polysulfide intermediates and the terminal sodium sulfide product.
Parameter	E/S	Electrolyte-to-sulfur ratio, reported as electrolyte volume per sulfur mass.
Parameter	N/P	Negative-to-positive capacity ratio, used here to describe sodium excess relative to cathode capacity.
Unit	M	Molar concentration, mol L^{-1}.
Unit	V	Voltage, volt.
Unit	°C	Temperature in degrees Celsius.
Unit	mg cm^{-2}	Areal mass loading, particularly sulfur loading.
Unit	μL mg^{-1}	Electrolyte volume per sulfur mass, used for E/S.
Unit	mAh g^{-1}	Gravimetric specific capacity.
Unit	mAh cm^{-2}	Areal capacity.
Unit	mA g^{-1}/A g^{-1}	Gravimetric current density.
Unit	Wh kg^{-1}	Gravimetric specific energy or energy density, depending on the stated normalization basis.

References

1. Seh, Z.W.; Sun, Y.; Zhang, Q.; Cui, Y. Designing high-energy lithium-sulfur batteries. *Chem. Soc. Rev.* **2016**, *45*, 5605–5634. [CrossRef] [PubMed]
2. Thangaraj, B.; Chuangchote, S.; Wongyao, N.; Solomon, P.R.; Roongraung, K.; Chaiworn, W.; Surareungchai, W. Flexible sodium-ion batteries using electrodes from Samanea saman tree leaf-derived carbon quantum dots decorated with SnO_2 and $NaVO_3$. *Clean. Energy* **2021**, *5*, 354–374. [CrossRef]
3. Wu, Y.; Huang, J.; Zhang, Z.; Chen, D.; Yu, H.; Ma, F.; Zhang, X.; Chen, Y. Recent advances in functionalized separators for shuttle-free and dendrite-free lithium/sodium-sulfur batteries. *Energy Mater.* **2025**, *5*, 500027. [CrossRef]
4. Wang, Y.-X.; Zhang, B.; Lai, W.; Xu, Y.; Chou, S.-L.; Liu, H.-K.; Dou, S.-X. Room-Temperature Sodium-Sulfur Batteries: A Comprehensive Review on Research Progress and Cell Chemistry. *Adv. Energy Mater.* **2017**, *7*, 1602829. [CrossRef]
5. Guo, Q.; Sun, S.; Kim, K.-I.; Zhang, H.; Liu, X.; Yan, C.; Xia, H. A novel one-step reaction sodium-sulfur battery with high areal sulfur loading on hierarchical porous carbon fiber. *Carbon Energy* **2021**, *3*, 440–448. [CrossRef]
6. Liu, Y.; Ma, S.; Rosebrock, M.; Rusch, P.; Barnscheidt, Y.; Wu, C.; Nan, P.; Bettels, F.; Lin, Z.; Li, T.; et al. Tungsten Nanoparticles Accelerate Polysulfides Conversion: A Viable Route toward Stable Room-Temperature Sodium-Sulfur Batteries. *Adv. Sci.* **2022**, *9*, 2105544. [CrossRef] [PubMed]
7. Wen, Z.; Cao, J.; Gu, Z.; Xu, X.; Zhang, F.; Lin, Z. Research on sodium sulfur battery for energy storage. *Solid State Ion.* **2008**, *179*, 1697–1701. [CrossRef]
8. Wang, Y.-X.; Lai, W.-H.; Chou, S.-L.; Liu, H.-K.; Dou, S.-X. Remedies for Polysulfide Dissolution in Room-Temperature Sodium-Sulfur Batteries. *Adv. Mater.* **2020**, *32*, 1903952. [CrossRef] [PubMed]
9. Wang, N.; Wang, Y.; Bai, Z.; Fang, Z.; Zhang, X.; Xu, Z.; Ding, Y.; Xu, X.; Du, Y.; Dou, X.; et al. High-performance room-temperature sodium–sulfur battery enabled by electrocatalytic sodium polysulfides full conversion. *Energy Environ. Sci.* **2020**, *13*, 562–570. [CrossRef]
10. Jin, F.; Wang, B.; Wang, J.; Wang, Y.; Ning, Y.; Yang, J.; Zhang, Z.; Liu, P.; Zhou, Y.; Wang, D.; et al. Boosting electrochemical kinetics of S cathodes for room temperature Na/S batteries. *Matter* **2021**, *4*, 1768–1800. [CrossRef]
11. Wei, S.; Xu, S.; Agrawral, A.; Choudhury, S.; Lu, Y.; Tu, Z.; Ma, L.; Archer, L.A. A stable room-temperature sodium-sulfur battery. *Nat. Commun.* **2016**, *7*, 11722. [CrossRef] [PubMed]
12. Jin, F.; Wang, R.; Liu, Y.; Zhang, N.; Bao, C.; Li, D.; Wang, D.; Cheng, T.; Liu, H.; Dou, S.; et al. Conversion mechanism of sulfur in room-temperature sodium-sulfur battery with carbonate-based electrolyte. *Energy Storage Mater.* **2024**, *69*, 103388. [CrossRef]
13. Zhang, Y.; Guo, X.; Yang, Q.; Shao, Y.; Du, Y.; Qi, J.; Zhao, M.; Shang, Z.; Hao, Y.; Tang, Y.; et al. Chemical and spatial dual-confinement engineering for stable Na–S batteries with approximately 100% capacity retention. *Proc. Natl. Acad. Sci. USA* **2023**, *120*, e2314408120. [CrossRef] [PubMed]
14. Wang, Y.; Lai, Y.; Chu, J.; Yan, Z.; Wang, Y.-X.; Chou, S.-L.; Liu, H.-K.; Dou, S.-X.; Ai, X.; Yang, H.; et al. Tunable Electrocatalytic Behavior of Sodiated MoS_2 Active Sites toward Efficient Sulfur Redox Reactions in Room-Temperature Na–S Batteries. *Adv. Mater.* **2021**, *3*, 2100229. [CrossRef] [PubMed]
15. Dong, C.; Zhou, H.; Liu, H.; Jin, B.; Wen, Z.; Lang, X.; Li, J.; Kim, J.; Jiang, Q. Inhibited shuttle effect by functional separator for room-temperature sodium-sulfur batteries. *J. Mater. Sci. Technol.* **2022**, *113*, 207–216. [CrossRef]
16. Yu, X.; Li, H.; Liang, K.; Liu, S.; Li, L.; Zhu, Y.; Huang, H. Three-dimensional MXene coupled CoFe nanoalloys as sulfur host for long-life room-temperature sodium-sulfur batteries. *Energy Mater.* **2025**, *5*, 500086. [CrossRef]
17. Dong, C.; Han, Z.; Su, Z.; Dong, Y.; Chen, Q.; He, G.; Sun, X.; Zhang, N.; Jiang, Q.; Pu, X. "One stone-two birds": Reviving waste-activated carbon for stable polysulfide shuttle-free room-temperature Na–S batteries. *Energy Mater.* **2026**, *6*, 600055. [CrossRef]
18. Luo, S.; Ruan, J.; Wang, Y.; Hu, J.; Song, Y.; Chen, M.; Wu, L. Flower-Like Interlayer-Expanded MoS2-x Nanosheets Confined in Hollow Carbon Spheres with High-Efficiency Electrocatalysis Sites for Advanced Sodium-Sulfur Battery. *Small* **2021**, *17*, 2101879. [CrossRef] [PubMed]
19. Zhang, S.; Yao, Y.; Jiao, X.; Ma, M.; Huang, H.; Zhou, X.; Wang, L.; Bai, J.; Yu, Y. Mo2N-W2N Heterostructures Embedded in Spherical Carbon Superstructure as Highly Efficient Polysulfide Electrocatalysts for Stable Room-Temperature Na–S Batteries. *Adv. Mater.* **2021**, *33*, 2103846. [CrossRef] [PubMed]
20. Yang, Z.; Xiao, R.; Zhang, X.; Wang, X.; Zhang, D.; Sun, Z.; Li, F. Role of Catalytic Materials on Conversion of Sulfur Species for Room Temperature Sodium-Sulfur Battery. *Energy Environ. Mater.* **2022**, *5*, 693–710. [CrossRef]
21. Lei, Y.; Wu, C.; Lu, X.; Hua, W.; Li, S.; Liang, Y.; Liu, H.; Lai, W.-H.; Gu, Q.; Cai, X.; et al. Streamline sulfur redox reactions to achieve efficient roomtemperature sodium-sulfur batteries. *Angew. Chem. Int. Ed.* **2022**, *61*, e202200384. [CrossRef] [PubMed]
22. Wei, X.; Zhang, Z.; Luo, D.; Wang, X. Construction of Heterointerfaced Nanoreactor Electrocatalyst via In Situ Evolution Toward Practical Room-Temperature Sodium-Sulfur Batteries. *Adv. Funct. Mater.* **2025**, *35*, 2414172. [CrossRef]
23. Qi, Y.; Li, Q.-J.; Wu, Y.; Bao, S.-J.; Li, C.; Chen, Y.; Wang, G.; Xu, M. A Fe3N/carbon composite electrocatalyst for effective polysulfides regulation in room temperature Na–S batteries. *Nat. Commun.* **2021**, *12*, 6347. [CrossRef] [PubMed]

24. He, J.; Bhargav, A.; Su, L.; Charalambous, H.; Manthiram, A. Intercalation-type catalyst for non-aqueous room temperature sodium-sulfur batteries. *Nat. Commun.* **2023**, *14*, 6568. [CrossRef] [PubMed]
25. Guo, D.; Wang, J.; Lai, T.; Henkelman, G.; Manthiram, A. Electrolytes with Solvating Inner Sheath Engineering for Practical Na–S Batteries. *Adv. Mater.* **2023**, *35*, 2300841. [CrossRef] [PubMed]
26. Bai, R.; Yao, Y.; Lin, Q.; Wu, L.; Li, Z.; Wang, H.; Ma, M.; Mu, D.; Hu, L.; Yang, H.; et al. Preferable single-atom catalysts enabled by natural language processing for high energy density Na–S batteries. *Nat. Commun.* **2025**, *16*, 5827. [CrossRef] [PubMed]
27. Zheng, F.; Zhang, Y.; Li, Z.; Yao, G.; Wei, L.; Wang, C.; Chen, Q.; Wang, H. Axial ligand induces the charge localization of Ca single-atom sites for efficient Na–S batteries. *Nat. Commun.* **2025**, *16*, 4372. [CrossRef] [PubMed]
28. Zhang, B.-W.; Sheng, T.; Liu, Y.-D.; Wang, Y.-X.; Zhang, L.; Lai, W.-H.; Wang, L.; Yang, J.; Gu, Q.-F.; Chou, S.-L.; et al. Atomic cobalt as an efficient electrocatalyst in sulfur cathodes for superior room-temperature sodium-sulfur batteries. *Nat. Commun.* **2018**, *9*, 4082. [CrossRef] [PubMed]
29. Jagadeesan, S.N.; Hao, H.; Sinha, A.; Xue, Z.; Nanda, J.; Zheng, X. Elucidating sodium-sulfur battery chemistry using operando transmission X-ray microscopy and X-ray absorption spectroscopy. *J. Electrochem. Soc.* **2025**, *172*, 110508. [CrossRef]
30. Zhao, C.; Amine, K.; Xu, G.-L. Nontraditional Approaches To Enable High-Energy and Long-Life Lithium-Sulfur Batteries. *Acc. Chem. Res.* **2023**, *56*, 2700–2712. [CrossRef] [PubMed]
31. Park, H.; Jeon, C.; Kansara, S.; Lee, C.; Xiong, S.; Sun, Z.; Hwang, J.-Y. Investigating the effect of binder for stabilizing a sulfurized polyacrylonitrile cathode in sodium-sulfur batteries. *J. Power Sources* **2026**, *661*, 238587. [CrossRef]
32. Zheng, F.; Zhang, Y.; Ding, G.; Xiao, Y.; Wei, L.; Su, J.; Wang, C.; Chen, Q.; Wang, H. Pentagon Defects Accelerating Polysulfides Conversion Enabled High-Performance Sodium-Sulfur Batteries. *Adv. Funct. Mater.* **2024**, *34*, 2310598. [CrossRef]
33. Zhang, S.; Huang, M.; Wang, Y.; Wang, Z.; Wang, H.; Liu, X. Achieving a Quasi-Solid-State Conversion of Polysulfides via Building High Efficiency Heterostructure for Room Temperature Na–S Batteries. *Adv. Energy Mater.* **2024**, *14*, 2303925. [CrossRef]
34. Li, Z.; Chen, X.; Yao, G.; Wei, L.; Chen, Q.; Luo, Q.; Zheng, F.; Wang, H. Strengthening d-p Orbital-Hybridization via Coordination Number Regulation of Manganese Single-Atom Catalysts Toward Fast Kinetic and Long-Life Sodium-Sulfur Batteries. *Adv. Funct. Mater.* **2024**, *34*, 2400859. [CrossRef]
35. Li, C.; Yu, J.; Yang, D.; Li, H.; Cheng, Y.; Ren, Y.; Bi, X.; Ma, J.; Zhao, R.; Zhou, Y.; et al. Balancing Electronic Spin State via Atomically-Dispersed Heteronuclear Fe–Co Pairs for High-Performance Sodium-Sulfur Batteries. *J. Am. Chem. Soc.* **2025**, *147*, 8250–8259. [CrossRef] [PubMed]
36. Gao, W.; Su, L.; Yu, Y.; Lu, Y.; Liu, X.; Peng, Y.; Xiong, X.; He, J.; Chen, Y.; Wu, Y. Stable Dendrite-Free Room Temperature Sodium-Sulfur Batteries Enabled by a Novel Sodium Thiotellurate Interface. *Angew. Chem. Int. Ed.* **2024**, *63*, e202412287. [CrossRef] [PubMed]
37. Zhong, X.; Huang, Y.; Cai, J.; Li, Y.; He, Z.; Cai, D.; Geng, Z.; Deng, W.; Zou, G.; Hou, H.; et al. Origin of the high catalytic activity of MoS_2 in Na–S batteries: Electrochemically reconstructed Mo single atoms. *J. Am. Chem. Soc.* **2024**, *146*, 32124–32134. [CrossRef] [PubMed]
38. Liu, Y.; Lu, S.; Weng, S.; Xu, J.; Tu, H.; Wang, Z.; Xue, J.; Liu, L.; Zhang, F.; Sun, G.; et al. Interphase-Regulated Room-Temperature Sodium-Sulfur Batteries Enabled by a Nonflammable Dual-Functional Electrolyte. *Adv. Energy Mater.* **2025**, *15*, 2404890. [CrossRef]
39. Wang, L.; Ren, N.; Jiang, W.; Yang, H.; Ye, S.; Jiang, Y.; Ali, G.; Song, L.; Wu, X.; Rui, X.; et al. Tailoring Na^+ Solvation Environment and Electrode-Electrolyte Interphases with $Sn(OTf)_2$ Additive in Non-flammable Phosphate Electrolytes towards Safe and Efficient Na–S Batteries. *Angew. Chem. Int. Ed.* **2024**, *63*, e202320060. [CrossRef] [PubMed]
40. Weng, S.; Liu, Y.; Lu, S.; Xu, J.; Xue, J.; Tu, H.; Wang, Z.; Liu, L.; Gao, Y.; Sun, G.; et al. Unraveling the Multifunctional Mechanism of Fluoroethylene Carbonate in Enhancing High-Performance Room-Temperature Sodium-Sulfur Batteries. *Angew. Chem. Int. Ed.* **2025**, *64*, e202421602. [CrossRef] [PubMed]
41. Pai, M.-H.; Lai, T.; Manthiram, A. Sodium-Sulfur Cells with a Sulfurized Polyacrylonitrile Cathode and a Localized High Concentration Electrolyte with Toluene as a Nonfluorinated Diluent. *Adv. Funct. Mater.* **2024**, *34*, 2407450. [CrossRef]
42. Yao, W.; Pai, M.-H.; Manthiram, A. Deciphering the Impact of Polysulfide Solvation Structure on Electrical Double Layer Chemistry in Sodium-Sulfur Batteries. *Angew. Chem. Int. Ed.* **2025**, *64*, e202424547. [CrossRef] [PubMed]
43. Yao, W.; Pai, M.-H.; Manthiram, A. Inner-Outer Sheath Synergistic Shielding of Polysulfides in Asymmetric Solvent-Based Electrolytes for Stable Sodium-Sulfur Batteries. *J. Am. Chem. Soc.* **2025**, *147*, 12061–12074. [CrossRef] [PubMed]
44. Zou, Y.; Zhang, B.; Luo, H.; Yu, X.; Yang, M.; Zheng, Q.; Wang, J.; Jiao, C.; Chen, Y.; Zhang, H.; et al. Electrolyte Solvation Engineering Stabilizing Anode-Free Sodium Metal Battery with 4.0 V-Class Layered Oxide Cathode. *Adv. Mater.* **2024**, *36*, 2410261. [CrossRef] [PubMed]
45. Nguyen, H.Q.; Kanedal, M.D.; Todt, J.; Jin, F.; Do, Q.; Zalka, D.; Maximenko, A.; Stoian, D.; Schell, N.; van Beek, W.; et al. Revealing the Hidden Polysulfides in Solid-State Na–S Batteries: How Pressure and Electrical Transport Control Kinetic Pathways. *J. Am. Chem. Soc.* **2025**, *147*, 23492–23503. [CrossRef] [PubMed]

46. Guo, Y.; Liu, K.; Li, C.; Song, D.; Zhang, H.; Wang, Z.; Yan, Y.; Zhang, L.; Dai, S. A Sulfide-Based Solid Electrolyte with High Humid Air Tolerance for Long Lifespan All-Solid-State Sodium Batteries. *Adv. Energy Mater.* **2024**, *14*, 2401504. [CrossRef]
47. Deng, J.; Ren, X.; Lin, H.; Hu, L.; Bai, Y.; Yu, X.; Mo, J.; Zhang, Q.; Kang, F.; Li, B. Functionally gradient materials for sustainable and high-energy rechargeable lithium batteries: Design principles, progress, and perspectives. *J. Energy Chem.* **2024**, *99*, 426–449. [CrossRef]

Disclaimer/Publisher's Note: The statements, opinions and data contained in all publications are solely those of the individual author(s) and contributor(s) and not of MDPI and/or the editor(s). MDPI and/or the editor(s) disclaim responsibility for any injury to people or property resulting from any ideas, methods, instructions or products referred to in the content.